Acta Crystallographica Section A
Foundations of Crystallography
ISSN 0108-7673

Received 5 February 2002
Accepted 27 June 2002

A study on the position of boron atoms in $(Y_{0.6}Ca_{0.4})(SrBa)(Cu_{2.5}B_{0.5})O_{7-\delta}$

H. B. Wang,[a] H. Jiang,[a,b] F. H. Li,[a]* G. C. Che[c] and D. Tang[d]

[a]Institute of Physics and Center for Condensed Matter Physics, Chinese Academy of Sciences, PO Box 603, Beijing 100080, People's Republic of China, [b]Beijing Laboratory of Electron Microscopy, Institute of Physics and Center for Condensed Matter Physics, Chinese Academy of Sciences, PO Box 2724, Beijing 100080, People's Republic of China, [c]National Laboratory for Superconductivity, Institute of Physics and Center for Condensed Matter Physics, Chinese Academy of Sciences, PO Box 603, Beijing 100080, People's Republic of China, and [d]Application Lab, FEI Electron Optics, PO Box 80066, 5600 KA Eindhoven, The Netherlands. Correspondence e-mail: lifh@aphy.iphy.ac.cn

The position of boron atoms in minute crystals of $(Y_{0.6}Ca_{0.4})(SrBa)(Cu_{2.5}B_{0.5})O_{7-\delta}$ was studied by means of image processing based on the combination of high-resolution electron microscopy and electron diffraction. The structure image was obtained from a single image by image deconvolution based on the principle of maximum entropy. Its resolution is limited by that of the electron microscope. Then the image resolution was enhanced to about 1 Å by direct-methods phase extension in combination with an empirical method of electron diffraction intensity correction. To study the substitution of boron atoms for copper, in the second cycle of diffraction intensity correction two different structure models were proposed. The one corresponding to a more reasonable atomic shape in the derived projected potential map (PPM) was accepted. In this model, the boron atoms are located at the 'chain' Cu sites.

1. Introduction

The first reported boron-containing compound in the Y–Sr–Cu–O system, $YSr_2Cu_{3-x}B_xO_7$, is not a superconductor (Zhu *et al.*, 1993). Since then several series of related compounds have been synthesized for studying the property change caused by the element substitution (Zhu *et al.*, 1993; Li *et al.*, 1993; Slater & Greaves, 1993; Uehara *et al.*, 1993; Deng *et al.*, 1997; Che *et al.*, 2000). It was found that compounds $(R_{0.6}Ca_{0.4})(SrBa)(Cu_{2.5}B_{0.5})O_{7-\delta}$ (R = La, Nd, Sm, Eu, Gd, Y, Dy, Ho, Er, Tm and Yb) with the ratio of Cu and B atoms equal to 5:1 are high-temperature superconductors (Che *et al.*, 2000). Principally, the crystal structure of these compounds is isomorphic to that of $YBa_2Cu_3O_{7-\delta}$. It is recognized that the substitution for Cu means the replacement of Cu atoms located on the Cu—O chains by some other atoms (Sunshine *et al.*, 1989; Miyazaki *et al.*, 1992; Slater *et al.*, 1993). The crystal structure determination for $YSr_2Cu_{2.25}B_{0.75}O_{7-\delta}$ by neutron diffraction (Chapman & Attfield, 1994) confirms the substitution of B atoms for Cu atoms on the Cu—O chains.

Like most high-temperature superconducting oxides and related compounds, the crystals of $(Y_{0.6}Ca_{0.4})(SrBa)(Cu_{2.5}B_{0.5})O_{7-\delta}$, which are insufficiently large for X-ray single-crystal diffraction analysis, may be suitable samples for studying by electrons. Some techniques based on convergent-beam electron diffraction have been applied to the measurement of charge distribution in cuprate superconductors (Taftø *et al.*, 1998; Akase *et al.*, 2000). Although the scattering power of B atoms for electrons is very weak, compared with that of other atoms in the crystal, it is relatively stronger than that for X-rays. For instance, the crystal structure of boric acid was successfully studied by electron diffraction (Cowley, 1953; Dorset, 1992) and the boron atoms are seen clearly in the potential maps. The position of boron atoms in $La_3Ni_2B_2N_3$ and $ThPd_xB_{6-2x}$ were determined by the structure refinement from dynamical electron diffraction data (Jansen *et al.*, 1998). It would be interesting to see the possibility of determining positions of B atoms in the crystal structure of $(Y_{0.6}Ca_{0.4})(SrBa)(Cu_{2.5}B_{0.5})O_{7-\delta}$ *via* the interaction between the sample and electrons. The task is to make clear how the B atoms substitute for Cu atoms in the examined structure rather than to determine the crystal structure *ab initio*.

A two-stage electron crystallographic image-processing technique was set up to determine the structure of minute inorganic crystals with the resolution close to the diffraction resolution limit (Li, 1994, 1998). According to the weak-phase-object approximation (WPOA), the image intensity in high-resolution electron microscopy (HREM) is expressed as

$$I(\mathbf{r}) = 1 + 2\sigma\varphi(\mathbf{r}) * \mathcal{F}^{-1}[W(H)], \qquad (1)$$

where $\sigma = \pi/\lambda U$, λ is the wavelength and U the accelerating voltage of electrons, $\varphi(\mathbf{r})$ and $W(H)$ denote the projected potential distribution function (PPDF) and contrast transfer function, respectively, $*$ and $\mathcal{F}^{-1}$ represent the operator of convolution and the inverse Fourier transform, respectively. In

the first stage of image processing, an image that may not reflect the projected structure is transformed into the structure image by image deconvolution based on (1) (Han *et al.*, 1986; Hu & Li, 1991). The resolution of a such obtained structure image is limited by the microscope resolution, and hence not all atoms can be seen in the image, if a medium-voltage, for instance 200 kV, microscope is employed. Electron diffraction patterns (EDPs) usually contain rather high scattering-angle reflections. In the second stage of image processing, the corresponding electron diffraction data are introduced to improve the image resolution by phase extension using the direct method developed in X-ray crystallography (Fan *et al.*, 1985).

In the present paper, the two-stage image processing technique was applied to study the position of boron atoms in minute crystals of $(Y_{0.6}Ca_{0.4})(SrBa)(Cu_{2.5}B_{0.5})O_{7-\delta}$. The image deconvolution technique (Hu & Li, 1991) based on the principle of maximum entropy (Jaynes, 1957) was employed for image deconvolution and direct methods (Woolfson & Fan, 1995) for phase extension. An empirical method of electron diffraction intensity correction (Huang, Liu *et al.*, 1996) was applied to improve the quality of electron-diffraction data used for phase extension.

2. Experimental

A polycrystalline sample of $(Y_{0.6}Ca_{0.4})(SrBa)(Cu_{2.5}B_{0.5})O_{7-\delta}$ was prepared with dried Y_2O_3, $SrCO_3$, $BaCO_3$, $CaCO_3$, CuO and B_2O_3 powders of purity >99.99% as starting materials. These oxides in stoichiometric composition were mixed and ground thoroughly, then calcined at 1170 K in air for 40 h. The mixture was ground and pressed into pellets and sintered at about 1230 K in air for 50 h, cooled down to room temperature at the rate of 30K h^{-1} and then annealed in O_2 at 670 K for 40 h to improve the sample quality. The crystals were crushed in an agate mortar. The fine fractures were transferred onto a copper grid covered with a holey carbon film. The electron diffraction and HREM observations were carried out with JEM-200CX and JEM-2010 electron microscopes operated at 200 kV, respectively. The point resolution of JEM-2010 microscope is 1.94 Å. The electron diffraction intensities were collected by a slow-scan CCD camera equipped in a Tacnai F20 electron microscope operated at 200 kV. Experimental images were digitized by an Agfa scanner.

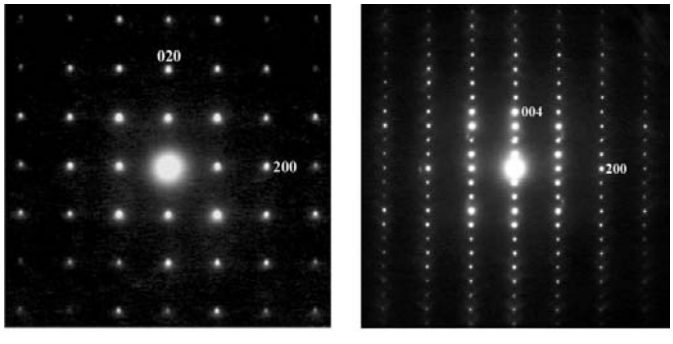

(*a*) (*b*)

Figure 1
(*a*) [001] and (*b*) [010] EDPs of $(Y_{0.6}Ca_{0.4})(SrBa)(Cu_{2.5}B_{0.5})O_{7-\delta}$.

3. Electron diffraction and image preprocessing

3.1. Lattice parameters

An electron diffraction study indicates that the unit cell is orthorhombic with the parameter *a* very close to *b*. Figs. 1(*a*) and 1(*b*) show the [001] and [010] EDPs, respectively. To determine the lattice parameters accurately, the holey carbon film is covered with an evaporated thin golden foil so that the diffraction spots of the examined sample and diffraction rings of polycrystalline gold are superimposed in the same pattern. The determined lattice parameters are $a = 3.85_4$, $b = 3.86_4$ and $c = 11.5_0$ Å. They are in agreement with the result given by X-ray diffraction (Che *et al.*, 2000).

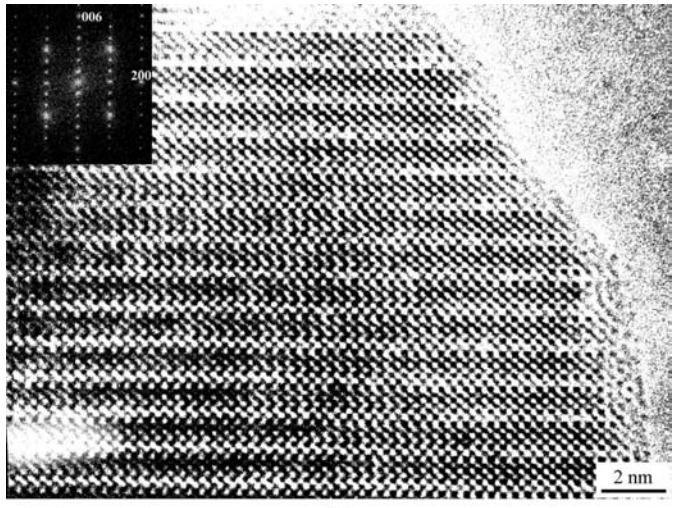

(*a*)

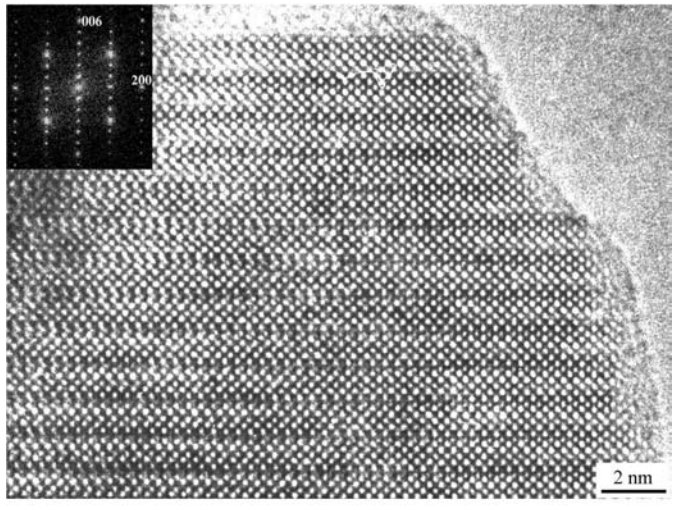

(*b*)

Figure 2
[010] images of $(Y_{0.6}Ca_{0.4})(SrBa)(Cu_{2.5}B_{0.5})O_{7-\delta}$ taken with different defocus conditions. The insets are corresponding diffractograms.

3.2. Fourier filtering and symmetry averaging

A series of [010] images were taken from the same area in the same sample with different defocus conditions. Two of them were selected for processing (see Fig. 2). Both of them were taken not very far from the Scherzer focus condition, and the defocus difference between them was set to be about 300 Å. The insets are corresponding diffractograms, namely, the Fourier transforms of images. The Fourier filtered images obtained from Figs. 2(*a*) and 2(*b*) are shown in Figs. 3(*a*) and 3(*b*), respectively. The contrast difference between them can be seen. The [010] EDP (Fig. 1*b*) shows an approximate *mm* symmetry, and no evidence of the extinction in it. In addition, the corresponding symmetry of compound $YBa_2Cu_3O_{7-\delta}$ is *p*2*mm*. Hence the symmetry of the [010] projected structure of $(Y_{0.6}Ca_{0.4})(SrBa)(Cu_{2.5}B_{0.5})O_{7-\delta}$ may also be *p*2*mm*. However, for reliability, the plane group was determined by comparing the minimum of total phase residuals (Hovmöller, 1992) among the plane groups *p*2*mm*, *p*2*mg* and *p*2*gg*. Each of the three plane groups gives rise to different phase relations. For each of them, the origin of the unit cell in Figs. 3(*a*) and 3(*b*) was selected such that the total phase residual has the minimum value. For the two images shown in Figs. 3(*a*) and 3(*b*), the average minimum phase residual corresponding to plane groups *p*2*mm*, *p*2*mg* and *p*2*gg* are 11.5, 13 and 14, respectively. Therefore, the [010] plane group of $(Y_{0.6}Ca_{0.4})(SrBa)(Cu_{2.5}B_{0.5})O_{7-\delta}$ is *p*2*mm*, *i.e.* the same as that of $YBa_2Cu_3O_{7-\delta}$, and the image averaging was performed with it. All these were carried out with the program *VEC* (Fan *et al.*, 2000). The average images for Figs. 3(*a*) and 3(*b*) are shown in Figs. 3(*c*) and 3(*d*), respectively. It can be seen that Figs. 3(*c*) and 3(*d*) are almost reversed to each other in contrast.

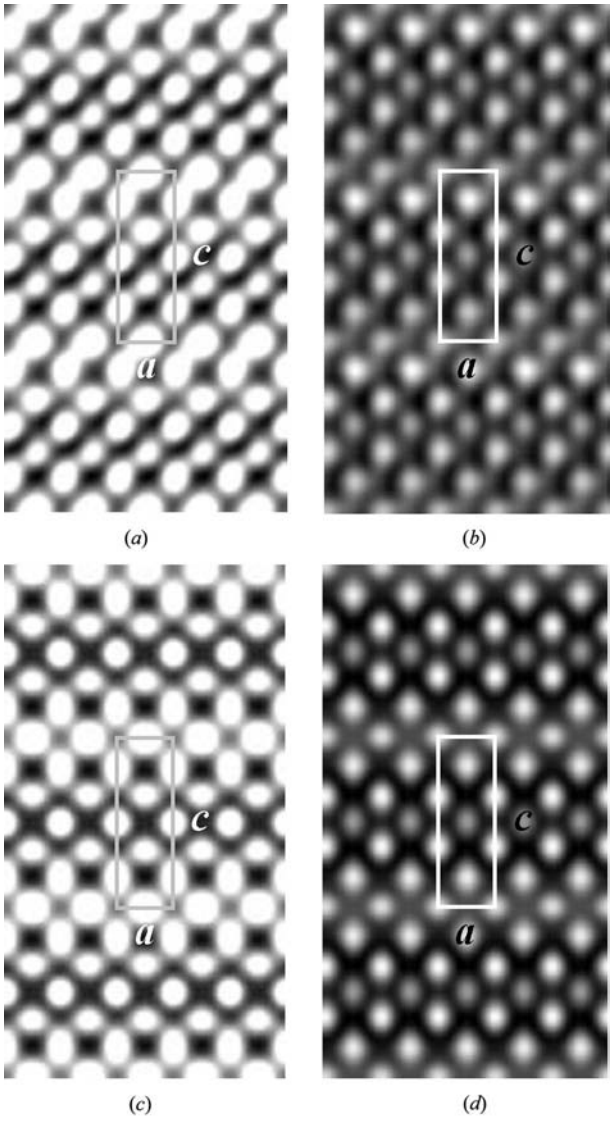

Figure 3
Fourier filtering images (*a*) and (*b*) and symmetry averaging images (*c*) and (*d*) corresponding to Figs. 2(*a*) and 2(*b*), respectively.

4. Maximum-entropy image deconvolution

4.1. Entropy-defocus curves and deconvoluted images

The maximum-entropy image deconvolution technique (Hu & Li, 1991) was employed in searching the experimental defocus values for images shown in Figs. 3(*c*) and 3(*d*). With reference to the experimental defocus condition, a series of trial defocus values were assigned from −1000 to 0 Å with the interval 10 Å. For each trial defocus, a projected potential map (PPM) was obtained and the value of the entropy was calculated from formulas

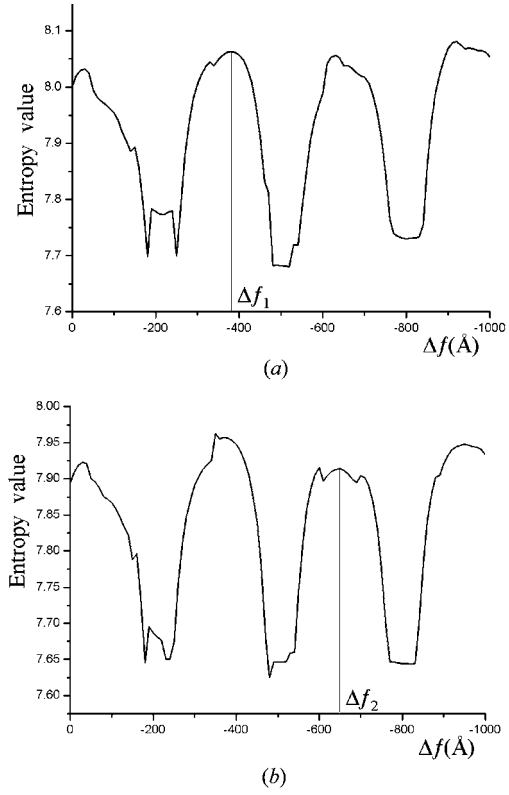

Figure 4
Entropy-defocus curves, (*a*) and (*b*) correspond to Figs. 3(*c*) and 3(*d*), respectively.

$$S = -\sum_{i=1}^{N} p_i \ln p_i \quad (2)$$

$$p_i = \phi_i \Big/ \sum_{i=1}^{N} \phi_i, \quad (3)$$

where ϕ_i denotes the value of the projected potential of the ith pixel. In principle, the PPM corresponding to the maximum entropy would be the correct one (Gull & Skilling, 1984).

Figs. 4(*a*) and 4(*b*) show the entropy–defocus curves corresponding to Figs. 3(*c*) and 3(*d*), respectively. There are four peaks in each curve. They correspond to defocus values −30, −380, −630 and −920 Å in Fig. 4(*a*) and correspond to −30, −370, −650 and −950 Å in Fig. 4(*b*). It was discussed in detail in a paper on the multisolution of maximum entropy image deconvolution (Huang, He & Li, 1996). For a more or less simple crystal structure, multiple peaks appear in the entropy–defocus curve with a more or less equal focus interval related to the Fourier images (Cowley & Moodie, 1957, 1960). In addition, some peaks of maximum entropy correspond to the true structure image, while others may correspond to the image reversed to the true one in contrast (Huang, He & Li, 1996). In the present case, the image deconvolution was carried out for all reasonable peaks. Because the image shown in Fig. 2(*b*) was taken at the farther underdefocus side than that shown in Fig. 2(*a*), the first peak from the right side in Fig. 4(*a*) and that from the left side in Fig. 4(*b*) were discarded. The deconvolution images are shown in Fig. 5, where (*a*), (*b*) and (*c*) are obtained from Fig. 3(*c*), and (*d*), (*e*) and (*f*) are from Fig. 3(*d*).

4.2. Structure images

The six deconvoluted images can be grouped into two types in contrast. The first type includes Figs. 5(*a*), 5(*c*), 5(*d*) and 5(*f*), and the second type includes Figs. 5(*b*) and 5(*e*). By

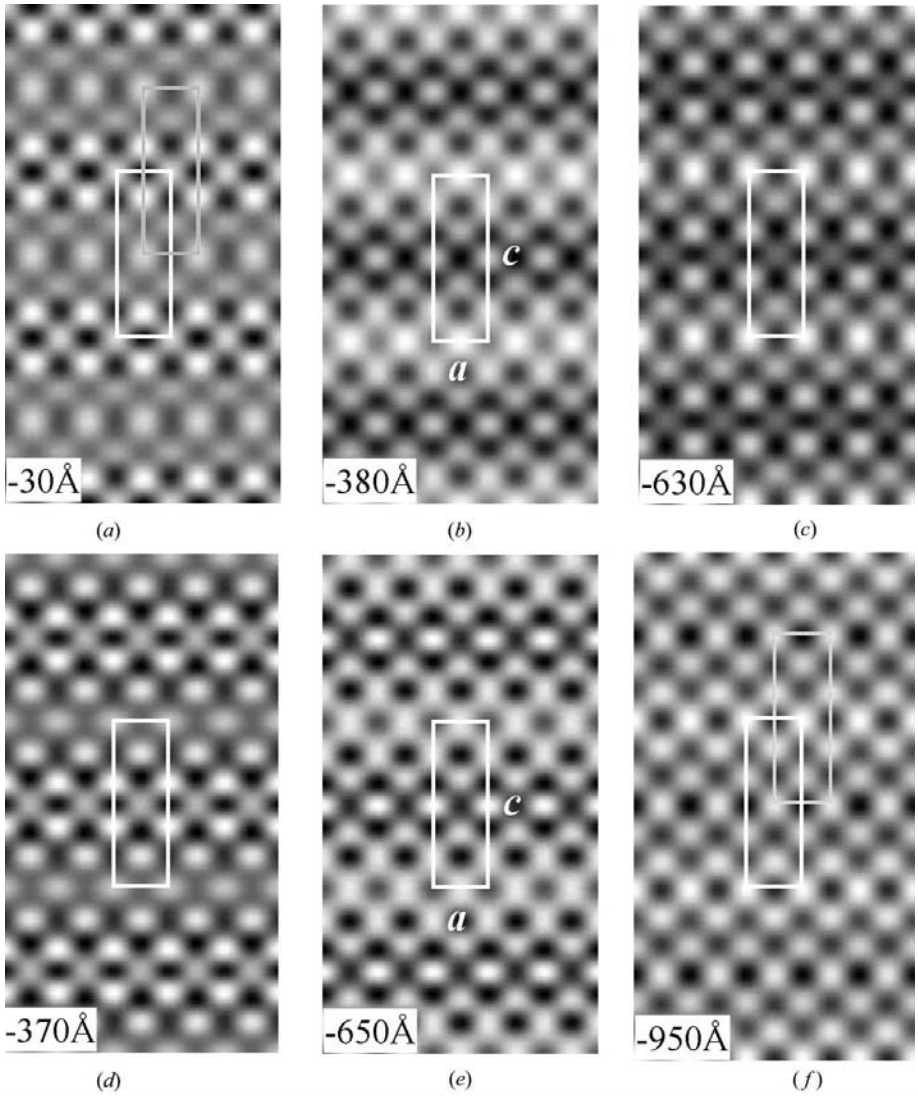

Figure 5
(*a*), (*b*) and (*c*) are deconvoluted images from Fig. 3(*c*) at defocus values −30, −380 and −630 Å, respectively. (*d*), (*e*) and (*f*) are deconvoluted images from Fig. 3(*d*) at defocus values −370, −650 and −950 Å, respectively. Rectangles indicate the projection of unit cells. The origins of the top right rectangles in (*a*) and (*f*) are shifted by a distance (**a** + **c**)/2 relative to the center rectangles.

Table 1
Phases of independent reflections obtained from the structure image.

No.	h	k	l	Phase
1	0	0	1	π
2	0	0	2	π
3	1	0	0	π
4	0	0	3	π
5	1	0	1	0.0
6	1	0	2	0.0
7	0	0	4	π
8	1	0	3	0.0
9	1	0	4	π
10	0	0	5	0.0

comparison with the crystal structure of $YBa_2Cu_3O_{7-\delta}$, it is found that all six images reflect the projected structure. In images of the first type, white dots represent metallic atoms though the positions of dots may slightly deviate from those of atoms, while in images of the second type black dots represent metallic atoms. This is in agreement with the argument given in Huang, He & Li (1996). However, atoms should appear black in structure images. Therefore, deconvoluted images given in Figs. 5(*b*) and 5(*e*) should be the structure images, while others are due to the Fourier image effect. Fig. 5(*b*) is similar to Fig. 3(*c*) in contrast, while Fig. 5(*e*) is almost reversed to Fig. 3(*d*). This is in agreement with the result of defocus determination that the image shown in Fig. 2(*a*) was taken close to the Scherzer focus condition, while Fig. 2(*b*) was taken relatively far from it.

By comparing Figs. 5(*a*), 5(*c*), 5(*d*) and 5(*f*), it can be seen that to shift the unit-cell origin in Figs. 5(*a*) and 5(*f*) in a distance equal to $(\mathbf{a}+\mathbf{c})/2$ (see the top right rectangle in gray) leads to a similar position configuration of white dots for the four pictures, though the brightness configuration in different pictures is different. This is again due to the Fourier image effect (Cowley & Moodie, 1957, 1960) and is discussed in Huang, He & Li (1996) in detail.

5. Phase extension and diffraction data correction

5.1. The general procedure

Phase extension was carried out by using the program *VEC* (Fan *et al.*, 2000). The initial set of structure-factor phases is obtained from the Fourier transform of the structure image and moduli from the square root of the electron diffraction data. The Fourier transform of the structure image shown in Fig. 5(*b*) yields 28 reflections in total, and the number of independent reflections is 10 (see Table 1). There are altogether 136 reflections in the recorded diffraction data up to 1 Å, and the number of symmetrically independent reflections is 41 (see Table 2).

To perform the phase-extension technique that is based on the kinematical diffraction theory, there must be a set of available electron diffraction intensities approximately proportional to the squares of structure factors. However, various factors such as Ewald-sphere curvature, non-flatness of specimen, crystal bending, lattice distortion, dynamical scattering and so on make the diffraction intensity deviate from the square structure factor. An empirical diffraction intensity correction method (Huang, Liu *et al.*, 1996) was reported to reduce the distortion of diffraction data. The procedure is as follows. Firstly, the partial structure factors $\mathbf{F}_p(\mathbf{H})$ containing only the contribution of atoms seen from the structure image are calculated. Secondly, divide the reciprocal space into a number of circular zones and the corrected intensity is obtained as

$$I_c(\mathbf{H})|_{\mathbf{H}_i\pm\Delta\mathbf{H}_i} = \frac{\langle|F_p(\mathbf{H})|^2\rangle_{\mathbf{H}_i\pm\Delta\mathbf{H}_i}}{\langle I_o(\mathbf{H})\rangle_{\mathbf{H}_i\pm\Delta\mathbf{H}_i}} I_o(\mathbf{H}), \qquad (4)$$

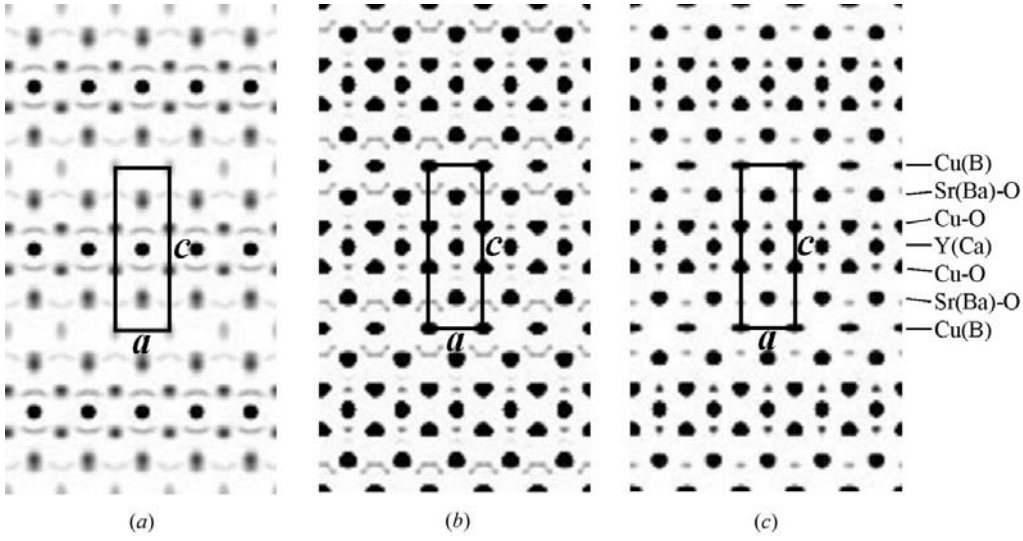

Figure 6
Projected potential maps obtained from Fig. 5(*b*) after phase extension in combination with the diffraction intensity correction for (*a*) one cycle, (*b*) and (*c*) two cycles. In the second cycle, the diffraction intensity correction for (*b*) was based on the structure model given in Fig. 7(*a*), while for (*c*) it was based on that given in Fig. 7(*b*).

Table 2
Square roots of observed and corrected diffraction intensities.

No.	h	k	l	$(I_o)^{1/2}$	$(I_c^{(1)})^{1/2}$	$(I_c^{(2)})^{1/2}$
1	0	0	1	16.138	10.450	6.024
2	0	0	2	11.803	7.075	4.852
3	1	0	0	14.305	8.828	5.477
4	0	0	3	16.944	9.816	7.558
5	1	0	1	12.307	11.804	5.431
6	1	0	2	10.009	9.763	8.120
7	0	0	4	13.382	13.561	11.856
8	1	0	3	17.089	18.005	18.624
9	1	0	4	11.158	13.740	12.294
10	0	0	5	8.144	10.706	11.810
11	1	0	5	7.181	10.040	11.139
12	2	0	0	15.016	18.416	24.318
13	0	0	6	10.041	12.610	15.194
14	2	0	1	7.366	8.669	10.925
15	2	0	2	5.862	6.909	5.761
16	2	0	3	8.563	7.982	4.627
17	1	0	6	7.944	4.721	4.638
18	0	0	7	10.480	7.669	6.530
19	2	0	4	6.447	4.595	5.807
20	1	0	7	6.881	6.490	6.593
21	2	0	5	4.962	5.372	6.375
22	0	0	8	7.052	8.015	10.079
23	2	0	6	5.313	6.189	7.948
24	1	0	8	5.703	7.055	7.302
25	3	0	0	4.575	5.384	6.481
26	0	0	9	5.690	7.836	5.768
27	3	0	1	3.190	4.501	2.900
28	3	0	2	3.049	4.245	3.967
29	2	0	7	4.997	7.149	6.993
30	3	0	3	5.974	9.133	8.570
31	1	0	9	3.913	6.136	5.596
32	3	0	4	3.811	5.900	5.238
33	2	0	8	3.539	5.628	3.546
34	0	0	10	3.875	4.762	4.571
35	3	0	5	2.809	3.050	3.125
36	1	0	10	4.490	5.868	5.378
37	3	0	6	2.892	4.046	4.613
38	2	0	9	2.610	3.473	4.399
39	0	0	11	3.216	4.542	4.894
40	3	0	7	2.198	2.875	3.767
41	1	0	11	2.995	4.266	5.270

I_o: observed diffraction intensity; $I_c^{(1)}$: diffraction intensity after correction for one time; $I_c^{(2)}$: diffraction intensity after correction for two times.

where I_o and I_c denote the observed and corrected intensities, respectively, $\mathbf{H}_i$ is the average value of $\mathbf{H}$ in the ith zone, $\Delta\mathbf{H}_i$ the half-width of the ith zone and $\langle\rangle$ denotes averaging. Then the phase extension was carried out by using the corrected diffraction amplitudes, and more atoms appear in the obtained PPM. After that a new set of partial structure factors was calculated and the observed intensity was scaled for another cycle, until all atoms appear in a stable potential map.

5.2. The first cycle

The peaks of corresponding black dots in Figs. 5(*b*) and 5(*e*) have the same positions, and the phases of corresponding reflections obtained from the Fourier transform of Figs. 5(*b*) and 5(*e*) are identical. Starting from the structure image shown in Fig. 5(*b*), a structure model containing all atoms except those of oxygen was proposed, in which the B atoms replace the Cu atoms randomly. The diffraction intensities were corrected on the basis of this model, and both $|F_p(\mathbf{H})|$ and $|I_o(\mathbf{H})|$ for each $\mathbf{H}$ are averaged with a certain number of neighbor reflections. Obviously, the corrected diffraction intensities depend on the number of neighbor reflections used for averaging. The right number was decided by comparing the phase-extension result with the average image and the knowledge of crystallographic chemistry as well. The PPM obtained by phase extension is shown in Fig. 6(*a*), where all atoms including O atoms are seen, though those of oxygen are diffuse.

5.3. The second cycle

Because the diffraction intensity used for phase extension always deviates from the square structure factor, the atomic

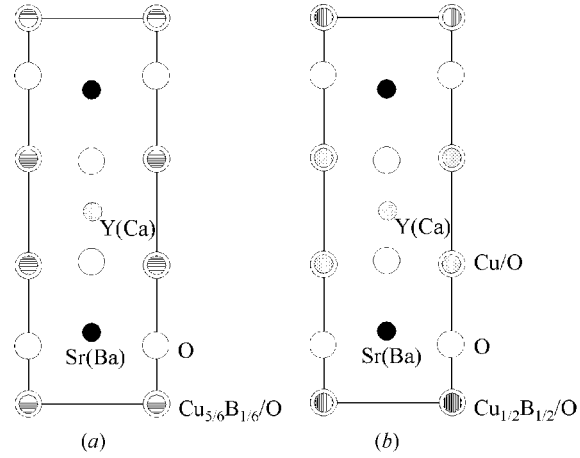

Figure 7
Structure models with (*a*) B atoms substituting for Cu atoms randomly and (*b*) B atoms substituting only for those Cu atoms that are on the Cu—O chains.

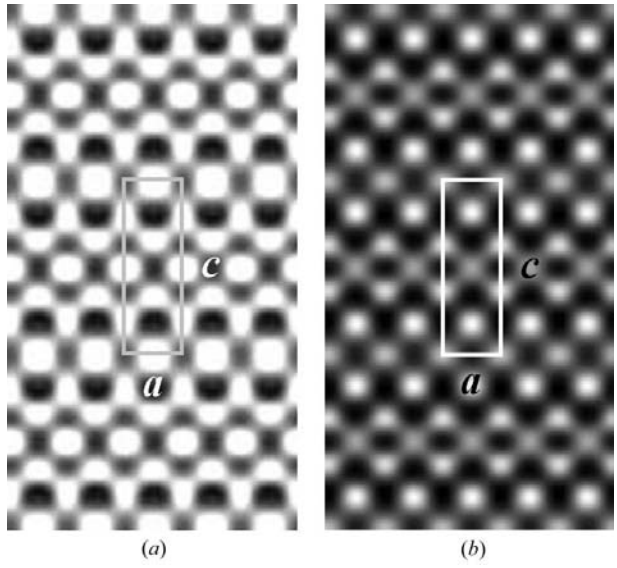

Figure 8
Simulated images of $(Y_{0.6}Ca_{0.4})(SrBa)(Cu_{2.5}B_{0.5})O_{7-\delta}$ with accelerating voltage 200 kV, spherical aberration coefficient 0.5 mm, standard deviation of Gaussian distribution of defocus due to the chromatic aberration 100 Å, crystal thickness 46.32 Å and defocus amount of (*a*) $\Delta f = -380$ Å and (*b*) $\Delta f = -650$ Å.

Table 3
Atomic coordinates for $(Y_{0.6}Ca_{0.4})(SrBa)(Cu_{2.5}B_{0.5})O_{7-\delta}$.

Atom	Site	x	z
Y(Ca)	1(*h*)	0.5	0.5
Sr(Ba)	2(*t*)	0.5	0.1883
Cu(B)	1(*a*)	0	0
Cu	2(*q*)	0	0.3589
O(1)	1(*e*)	0	0
O(2)	2(*q*)	0	0.1569
O(3*A*)	2(*s*)	0.5	0.3765
O(3*B*)	2(*r*)	0	0.3765

contrast in the determined PPM is not linear with the atom weight. This makes it difficult to study the atomic substitution. In addition, the electron diffraction data correction is aimed at approximating the diffraction intensity to the square structure factor of the model. Obviously, the success of diffraction-data correction depends to a great extent on the proposed structure model. So does the result of phase extension. It can be expected that a better fit of the proposed model to the true structure would lead to a better result for phase extension. Therefore, in the present case, two structure models containing all atoms including oxygen were constructed. In one of them, the B atoms substitute for Cu atoms randomly (Fig. 7*a*), while in the other the B atoms substitute for Cu atoms that are located in Cu—O chains (Fig. 7*b*). In both models, the positions of all O atoms are arranged at the center of the corresponding diffuse arc (see Fig. 6*a*). The second cycle of diffraction data correction was based on the two models, respectively. The phase extension was carried out with the two sets of corrected diffraction data, respectively. The obtained PPM based on the model shown in Fig. 7(*a*) is given in Fig. 6(*b*), and that based on the model shown in Fig. 7(*b*) is in Fig. 6(*c*). It can be seen that Fig. 6(*c*) is more reasonable than Fig. 6(*b*) in the appearance of the oxygen atoms. This means that the model given in Fig. 7(*b*) is more approximate to the true structure than that given in Fig. 7(*a*), and that the B atoms replace those Cu atoms which are located at Cu—O chains. The observed independent diffraction amplitudes and the amplitudes after the first and second cycles of correction are listed in Table 2. The atomic coordinates of the crystal are given in Table 3.

6. Image simulation

Image simulations based on the multislice theory were performed to confirm the proposed model (Fig. 7*b*). The electron optical parameters used in the calculation are the accelerating voltage 200 kV, spherical aberration coefficient 0.5 mm, standard deviation of Gaussian distribution of defocus owing to the chromatic aberration 100 Å. The defocus range is from −350 to −410 Å and also from −620 to −680 Å with step 5 Å, and crystal thickness range from 38.6 to 54.04 Å. Fig. 8 shows simulated images calculated with the crystal thickness 46.32 Å and the defocus amount of −380 and −650 Å, respectively. It can be seen that the calculated images match the experimental average images shown in Figs. 3(*c*) and 3(*d*).

7. Concluding remarks

The position of boron atoms in the minute crystal of $(Y_{0.6}Ca_{0.4})(SrBa)(Cu_{2.5}B_{0.5})O_{7-\delta}$, which is isomorphic to $YBa_2Cu_3O_{7-\delta}$, has been studied by using the two-stage image-processing technique based on the combination of high-resolution electron microscopy and electron diffraction. The work concentrates on studying how the B atoms substitute for Cu atoms in the structure rather than to determine the crystal structure *ab initio*. All atoms including oxygen are resolved in the final image and the boron atoms were determined to be located at the 'chain' Cu sites. The determined structure model was confirmed by image simulation.

It has been shown that, for the present compound, to set up two structure models in the process of phase extension in combination with electron diffraction data correction is beneficial for studying the atomic substitution of B for Cu. It can be expected that to have two or more structure models available might help to solve such problems for compounds of related series.

This project is supported by the National Natural Science Foundation of China and the Ministry of Sciences and Technology of China (NKBRSF-G1999064603).

References

Akase, Z., Tomokiyo, Y., Tanaka, Y. & Watanabe, M. (2000). *Physica (Utrecht) C*, **338,** 137–143.
Chapman, J. P. & Attfield, J. P. (1994). *Physica (Utrecht) C*, **235–240**, 351–352.
Che, G. C., Liu, G. D., Wu, F., Chen, H., Jia, S. L., Dong, C. & Zhao, Z. X. (2000). *Physica (Utrecht) C*, **341–348**, 391–394.
Cowley, J. M. (1953). *Acta Cryst.* **6**, 522–529.
Cowley, J. M. & Moodie, A. F. (1957). *Proc. Phys. Soc. London Ser. B*, **70**, 486–513.
Cowley, J. M. & Moodie, A. F. (1960). *Proc. Phys. Soc. London*, **76**, 378–384.
Deng, H., Dong, C., Shen, J. C., Wu, F., Chen, H., Jia, S. L., Che, G. C. & Zhao, Z. X. (1997). *Physica (Utrecht) C*, **278**, 107–112.
Dorset, D. L. (1992). *Acta Cryst.* A**48**, 568–574.
Fan, H. F., Wan, Z. H., Liu, Y. D., Fu, Z. Q., Li, Y. & Li, F. H. (2000). Proceedings of International Kunming Symposium on Microscopy, Kunming, pp. 45–46.
Fan, H. F., Zhong, Z. Y., Zheng, C. D. & Li, F. H. (1985). *Acta Cryst.* A**41**, 163–165.
Gull, S. F. & Skilling, J. (1984). *IEE Proc.* **131**, Part F, 646–659.
Han, F. S., Fan, H. F. & Li, F. H. (1986). *Acta Cryst.* A**42**, 353–356.
Hovmöller, S. (1992). *Ultramicroscopy*, **41**, 121–135.
Hu, J. J. & Li, F. H. (1991). *Ultramicroscopy*, **35**, 339–350.
Huang, D. X., He, W. Z. & Li, F. H. (1996). *Ultramicroscopy*, **62**, 141–148.
Huang, D. X., Liu, W., Gu, Y. X., Xiong, J. W., Fan, H. F. & Li, F. H. (1996). *Acta Cryst.* A**52**, 152–157.
Jansen, J., Tang, D., Zandbergen, H. W. & Schenk, H. (1998). *Acta Cryst.* A**54**, 91–101.
Jaynes, E. T. (1957). *Phys. Rev.* **106**, 620–630.

Li, F. H. (1994). Proc. 13th Int. Congr. Electron Microsc., Paris, Vol. 1, pp. 481–484.
Li, F. H. (1998). *Microscopy Res. Tech.* **40**, 86–100.
Li, J. Q., Li, F. H. & Zhao, Z. X. (1993). *Phys. Rev. B*, **48**, 1333–1336.
Miyazaki, Y., Yamane, H., Ohnishi, N., Kajitani, T., Hiraga, K., Morii, Y., Funahashi, S. & Hirai, T. (1992). *Physica (Utrecht) C*, **198**, 7–13.
Slater, P. R. & Greaves, C. (1993). *Physica (Utrecht) C*, **215,** 191–194.
Slater, P. R., Greaves, C., Slaski, M. & Muirhead, C. M. (1993). *Physica (Utrecht) C*, **208**, 193–196.
Sunshine, S. A., Schneemeyer, L. F., Siegrist, T., Douglass, D. C., Waszczak, J. V., Cava, R. J., Gyorgy, E. M. & Murphy, D. W. (1989). *Chem. Mater.* **1**, 331–335.
Taftø, J., Zhu, Y. M. & Wu, L. J. (1998). *Acta Cryst.* A**54**, 532–542.
Uehara, M., Nakata, H. & Akimitsu, J. (1993). *Physica (Utrecht) C*, **216**, 453–457.
Woolfson, M. M. & Fan, H. F. (1995). *Physical and Non-physical Methods in Solving Crystal Structure.* Cambridge University Press.
Zhu, W. J., Yue, J. J., Huang, Y. Z. & Zhao, Z. X. (1993). *Physica (Utrecht) C*, **205**, 118–122.